Three-dimensional printing of tissue phantoms for biophotonic imaging

Jianting Wang,[1,2] James Coburn,[2] Chia-Pin Liang,[1] Nicholas Woolsey,[1] Jessica C. Ramella-Roman,[3] Yu Chen,[1,2] and T. Joshua Pfefer[2,*]

[1]*Fischell Department of Bioengineering, University of Maryland, College Park, Maryland 20742, USA*

[2]*Center for Devices and Radiological Health, Food and Drug Administration, Silver Spring, Maryland 20993, USA*

[3]*Department of Biomedical Engineering, Florida International University, Miami, Florida 33174, USA*

Corresponding author: joshua.pfefer@fda.hhs.gov

We have investigated the potential of tissue phantoms fabricated with thermosoftening- and photopolymerization-based three-dimensional (3D) printers for use in evaluation of biophotonic imaging systems. The optical properties of printed polymer samples were measured and compared to biological tissues. Phantoms with subsurface channels as small as 0.2 mm in diameter were fabricated and imaged with microscopy, x-ray microtomography, and optical coherence tomography to characterize morphology. These phantoms were then implemented to evaluate the penetration depth of a hyperspectral reflectance imaging system used in conjunction with a near-infrared contrast agent. Results indicated that 3D printing may provide a suitable platform for performance testing in biophotonics, although subsurface imaging is critical to mitigate printer-to-printer variability in matrix homogeneity and feature microstructure.   © 2014 Optical Society of America

OCIS codes: (110.4234) Multispectral and hyperspectral imaging; (120.4800) Optical standards and testing; (170.3880) Medical and biological imaging; (170.7050) Turbid media.
http://dx.doi.org/10.1364/OL.39.003010

Phantom-based test methods form the foundation of guidance documents and standards for established medical imaging modalities, such as ultrasound and x-ray computed tomography (CT) [1,2]. These objective, quantitative methods are useful for system development, characterization, and intercomparison, as well as standardization of clinical trials, manufacturing quality control, and recalibration. However, in spite of extensive work in tissue-simulating phantoms [2], standardized methods for assessing biophotonic imaging system performance have not been established. Turbid phantoms that are well defined, biologically relevant, and durable are needed to achieve this goal. Such phantoms must be able to incorporate inclusions of varying depths and sizes in order to assess image quality characteristics such as penetration depth, and detectability. For technologies such as hyperspectral imaging, there is a need to visualize structures on the order of 100 microns [3]. However, fabrication of phantoms with fine spatial features can be complex and costly, involving processes such as spin coating [4], and photolithography [5]. Rapid prototyping with three-dimensional (3D) printing has brought significant promise as a fast, simple, and flexible way to produce such phantoms [2,6]. 3D printing uses digital data such as computer-aided design (CAD) files, decomposes the virtual object into a sequence of slices and builds the object layer by layer. CAD files can be designed manually or converted from image volumes (e.g., CT scans) to represent realistic tissue anatomy [6,7]. Thermoplastics and photopolymers are common printing media, although a variety of other materials have also been used [8].

Prior art on 3D printing of phantoms for biophotonics is limited to a study of curvature correction in spatial frequency domain imaging [9], which included optical property measurements of acrylonitrile butadiene styrene (ABS) polymer phantoms. In recent years, 3D printed phantoms have also been developed for applications in microwave breast imaging [7] and x-ray imaging [10]. While these studies represent significant steps, no prior work has explored the use of 3D printed phantoms with inclusions for characterizing biophotonic device performance. Furthermore, many questions remain regarding polymer optical properties, fabrication of microscale features, matrix homogeneity, and general practicality of these phantoms for imaging.

The purpose of this study was to evaluate the potential of 3D printing as a platform for fabricating phantoms that can be used as part of quantitative, objective test methods. Specifically, our goals were to design and fabricate phantoms for hyperspectral reflectance imaging (HRI), determine the optical properties of the polymer matrix materials, assess phantom morphology, and identify problem areas and directions for future research.

Phantoms generated with two printers—a lower resolution system based on thermosoftening and a higher resolution system based on photopolymerization—were studied. The first 3D printer (uPrint SE, Stratsys) employed an additive production process (Fused Filament Fabrication) to build ABS structures (ABS-M30). ABS is a thermoplastic polymer that is inexpensive and resistant to biological fluids. ABS is applied to a base material in sequential layers with a moving extrusion head. Phantoms were printed with zero nominal void volume, and no support material was used when creating internal channels. Under standard conditions each layer was 265 ± 5 μm thick. However, since no support material was used, the thickness of a layer tended to increase before hardening if not supported, such as in regions above channels. Consequently, actual channel dimensions and depths deviated from the nominal layer thicknesses in some samples. While channel widths specified as 100–300 μm were measured to be 350–500 μm, the measured dimensions were reproducible to a precision of

approximately ±60 µm. The other printer used was based on an additive polymer jetting process (Objective30, Objet Geometries Ltd.). It uses an array of inkjet print heads to deposit drops of liquid photopolymers to form each layer of a part, and the deposited photopolymer is cured by a UV light. Channels are created with wax-based supporting parts in the void region. The support materials are removed at the end of the fabrication. Two build materials were investigated—a white, polypropylene-like, low turbidity photopolymer (LTPP), and a resin-like, high turbidity photopolymer (HTPP). The printer features a higher resolution—horizontal build layer of 28 µm, with 100 µm lateral accuracy.

Optical properties of the three polymer samples were measured using the inverse adding-doubling (IAD) method [11], which involved measurement of transmittance and reflectance spectra using a spectrophotometer with an integrating sphere (Lambda 1050 UV/Vis/NIR, Perkin Elmer, Inc.). Thin sheets (0.6 mm thickness) of each polymer were printed for the measurements. IAD software (Oregon Medical Laser Center) was then used to calculate the absorption (μ_a) and reduced scattering coefficients (μ_s') over the wavelength range 400–1400 nm. μ_a and μ_s' values for the three polymers are graphed alongside data on human skin [12], human white brain matter [13], and bovine retina [14] for comparison (Fig. 1). The μ_s' values for ABS were greater than those of skin yet lower than those of white brain matter. The μ_s' of HTPP matches well with Caucasian skin in the visible range but is lower in the near-IR (NIR) range. The LTPP's μ_s' level is comparable to low-scattering tissues such as retina. The μ_a values for all the materials tended to be lower than those in biological tissue. In the future, it may be possible to improve the biological accuracy of phantom optical properties by incorporating chromophores or scatterers in the polymer prior to printing or in specific compartments of the phantom.

The phantoms studied here were designed to incorporate inclusions resembling blood vessels and structures used in phantoms for established medical imaging modalities [1]. Two types of phantom designs were fabricated —those incorporating channels at a constant size and various depths (from phantom surface to the top wall of the channel) and those with channels at a constant depth but varied size. The smallest channel size was limited by the resolution of the printers. For the thermosoftening printer, the channel depth was designed to be 0.5–1.4 mm, and the channels were designed to have square cross sections, in the size range of 0.35–0.5 mm. Given the higher resolution of the polymer-jetting-based
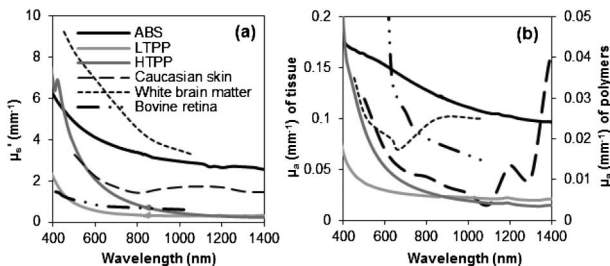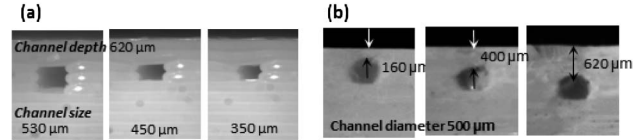

Fig. 2. Microscopy images on side surface (X–Z plane, $Y = 0$ mm) of (a) ABS phantoms with varied channel size and (b) LTPP phantoms with varied channel depth.

printer, cylindrical channels and smaller channel sizes and depths were attempted (size range 0.1–2 mm, depth range 0.2–2 mm). To facilitate injection of liquids to the channels, the channels were designed to include a uniform sized section (0.5 mm diameter) at both ends of each channel.

After printing, microscopy images of the phantom surfaces at the channel outlets were acquired (X–Z plane, $Y = 0$ mm). The ABS phantom shown in Fig. 2(a) exhibits stratification due to the layer-by-layer printing process. Sagging of the polymer prior to hardening caused scalloped features along the channel walls and an increase in the depth from the specified 0.5 to 0.62 mm. Figure 2(b) shows four of the channels of an LTPP phantom with varied channel depth. The layers printed were thinner and less visible than those of the ABS phantoms. The channel outlets are round in shape as designed. A depth of 160 µm was achieved.

X-ray micro-CT was used to provide full-phantom volumetric imaging. The voxel size of micro-CT is dependent on the sample size, as smaller samples can be placed within a smaller distance from the x-ray beam source, which allows a higher resolution. For the ABS phantom (2.5 cm × 1 cm × 1 cm), a voxel size of 20 µm was achieved. A 3D image of the phantom is shown in Fig. 3(a). The white pixels represent empty (air) space in the phantom. The channels are visible while aligned pores are also seen throughout the phantom. The phantom region (1 mm × 2 mm × 1 mm) in Fig. 3(b) shows a channel that is open to some of these pores, indicating a possibility for liquid leakage. Cross-sectional images of the ABS phantom are presented in Figs. 3(c)–3(e), where the white region is ABS, and the dark regions are empty spaces. These images reveal how strip-patterned ABS does not provide a seamless matrix.

Fig. 1. Optical properties of 3D-printed polymer samples compared to biological tissue [11–13]: (a) μ_s' and (b) μ_a.
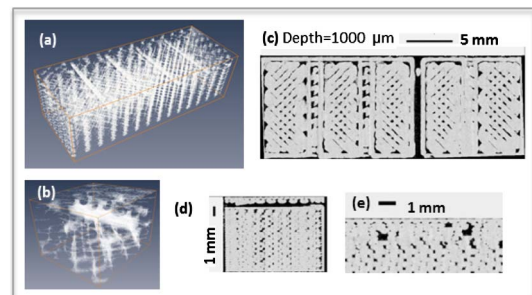

Fig. 3. Micro-CT images of an ABS phantom: 3D view of (a) full phantom (b) subvolume near a channel, where parts showing in white represents empty spaces (air), and cross-section view of (c) X–Y plane, 1 mm below the surface; (d) X–Z plane across a channel; and (e) Y–Z plane across two channels, where the dark region represents empty spaces (air).

In an attempt to create watertight channels, a postprinting sealing procedure was carried out. An acetone-wetted cotton thread was pulled through the channels to dissolve or soften small amounts of ABS at the channel wall and seal the gaps. After sealing, most channel walls became smoother; however, imaging with both HRI and micro-CT (not shown) indicated that not all channels were sealed and leakage could occur. Because of this inconsistency and the potential for undesired changes in channel morphology due to the acetone, we conclude that this approach is not suitable for sealing channels in ABS.

The micro-CT scan of the LTPP phantom (4.5 cm× 3 cm × 1 cm) has a voxel size of 49 μm. Figure 4(a) shows the 3D view of part of the phantom with four channels of different sizes. Figures 4(c) and 4(d) show the cross sections of channels designed to be 0.2–1.0 mm in diameter. In this phantom no pores or irregularities are observed. Micro-CT images indicated that the channel designed to be 0.1 mm diameter was not formed, suggesting that inclusions of this size are beyond the capacity of the printer for a reliable result. The channels that are designed to be 0.2 mm in diameter are shown in Figs. 4(b) and 4(c). One channel was found to be thinner than designed in the middle section [Fig. 4(c)]. It was also found that these small channels tend to get blocked after injection of water-based solutions. The channels that are 0.4 mm in diameter or larger are shown to be well constructed. Therefore, for the HTPP phantoms, all channels were designed no smaller than 0.4 mm. A micro-CT scan of the HTPP phantom indicated that all the channels were well fabricated to the design (data not shown).

Optical coherence tomography (OCT) can provide higher resolution imaging of subsurface features than micro-CT, but with lower penetration depth. Compared to micro-CT that gives contrast based on the density of an object, OCT contrast is based on the optical scattering property of the material. The OCT system used here (ThorLabs, Inc.) is a swept-source system with a broadband spectrum (100 nm wide, centered at 1300 nm). The laser operates at a sweep rate of 16 kHz with an average output power of 12 mW. The system sensitivity is 95 dB, and axial and lateral resolution levels are approximately 10 and 15 μm, respectively. A discrete Fourier transform is performed on the data to generate an axial depth profile of the sample with ∼3 mm imaging depth over 512 pixels.

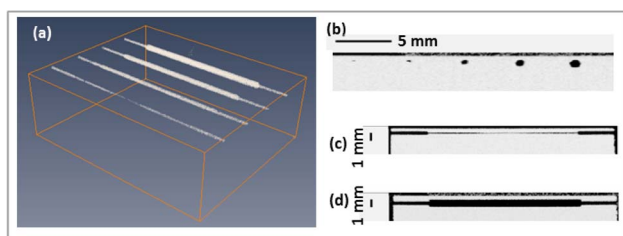Figure 5 shows cross-sectional OCT images of channels in the LTPP [Figs. 5(a)–5(d)] and HTPP
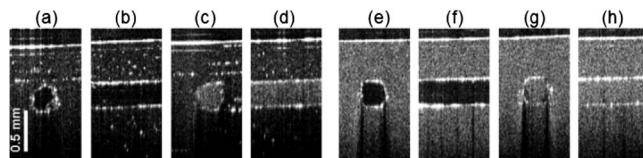

Fig. 5.   OCT images of (a)–(d) LTPP and (e)–(h) HTPP phantom. Channels filled with (a), (b), (e), (f) with water; (c), (d), (g), (h) with 1% Intralipid solution. (a), (c), (e), (g) X–Z plane; (b), (d), (f), (h) Y–Z plane.

[Figs. 5(e)–5(h)] phantoms. To minimize index of refraction change at the edge of the channels, water or 1% Intralipid solution was injected into the channels. For the LTPP phantom Intralipid solution increased μ_s' in the channel, providing a better contrast between the channel and the LTPP. For HTPP, water without scattering showed better contrast. Images show that scattering is homogeneous and low in the LTPP phantom and high in HTPP. The shape and interface of the channel are shown with high resolution.

The 0.2 mm channel in the LTPP phantom was examined by OCT, since its size is close to the resolution limit of micro-CT. Figures 6(a) and 6(b) and Figs. 6(c) and 6(d) show two different sections of the channel. In Figs. 6(a) and 6(b) the channel has a thickness of 140 μm; however, in Figs. 6(c) and 6(d) the thickness of the channel was reduced to 60 μm, while the width remains relatively constant. These images demonstrate that for structures exceeding the resolution of micro-CT, OCT can provide detailed feature examination.

As a preliminary evaluation of the utility of 3D printed phantoms as a platform for system assessment, we performed HRI measurements on an HTPP phantom. The HRI system includes a 100 W quartz tungsten–halogen light source (Oriel Instruments) for illumination. The surface of the phantom is illuminated at a ∼20° angle to the vertical, and the reflected light is filtered by a liquid crystal tunable filter (CRI Varispec, Perkin Elmer, Inc.) in the 650–1100 nm range, with a bandwidth of 10 nm. Images are captured by a Peltier-cooled, visible-NIR CCD camera (Princeton Instruments) with a macro zoom lens (Edmund Optics).

An NIR dye with a strong absorption peak at 770 nm, IR800 (LI-COR, Inc.), was used as a contrast agent for HRI imaging. IR800 has been used previously as an absorption contrast agent for diffuse optical tomography [15]. The channels of the HTPP phantom with 0.5 mm diameter and varied depth were filled with IR800 solutions at 1, 5, and 10 μM. Figure 7(a) shows an image of reflectance at 770 nm where the channels were filled with 10 μM IR800 solution. From left to right, the channel depth increases from 0.4 to 2.0 mm, and thus the detected contrast of the channel decreases.
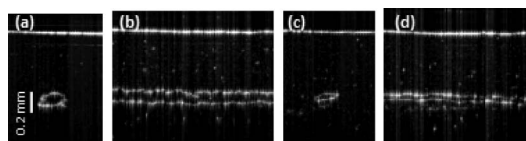

Fig. 4.   Micro-CT images of LTPP phantom with multisize channels: (a) 3D view, (b) X–Z plane showing five channels, and Y–Z plane along (c) 0.2 mm and (d) 1.0 mm channels.

Fig. 6.   Channel of 0.2 mm designed diameter: (a), (b) X–Z and Y–Z plane of a thicker section; (c), (d) X–Z and Y–Z plane of a thinner section.
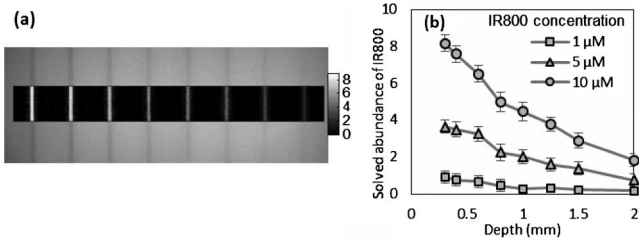
Fig. 7. Evaluation of imaging penetration depth with 3D printed phantom: (a) HRI image at 770 nm of HTPP phantom with 0.4–2.0 mm deep channels, filled with 10 μM IR800 dye, where overlay shows solved abundance (unitless) from spectral fitting; (b) Results for IR800 concentrations of 1, 5, and 10 μM.

The apparent absorbance at the location of the channel is extracted from measured reflectance by

$$A(\lambda) = \log[I(\lambda)/I_0(\lambda)], \tag{1}$$

where I is the measured reflectance at the region of interest (channel region) and I_0 is the reflectance at the reference region (nonchannel region). Thus, the absorbance spectrum at each pixel represents the spectral characteristics of optical constituents not present in the reference region (e.g., IR800, water). To quantify the component(s) of interest, it is assumed that the spectrum measured by HRI is a nonnegative linear summation of the absorption by each component in the channel. The nonnegative least square method is employed to perform spectral unmixing to solve for the relative abundance of each component, using the known extinction coefficient spectra [16]. In the middle of the image in Fig. 7(a) there is an overlay of IR800 abundance solved from the full data cube. Figure 7(b) shows results for IR800 solutions at three concentrations. We determined that for the 1 μM solution, the maximum penetration depth was 0.8 mm, based on a threshold signal-to-noise ratio value of 2.0. HRI measurements were also performed in ABS phantoms; however, poor results were obtained, as frequent problems with contrast agent diffusion into nonchannel regions were encountered.

Our findings indicate that 3D printing has significant potential as a method for fabricating phantoms for biophotonic applications. Materials with biologically relevant scattering coefficients and low absorption throughout the visible and NIR range are currently available, and it is expected that the scattering and absorption coefficient of the polymer can be tuned by adding scatterers and absorbers in the polymers prior to printing. The ability to achieve watertight channels with reliable morphology and sizes on the order of hundreds of micrometers varies from printer to printer. Therefore, the use of microscopy along with subsurface imaging techniques such as micro-CT—which provides superior penetration depth—and OCT—which provides higher resolution – can help to ensure quality. Our results also suggest that imaging may be useful for evaluating the morphology and mechanical integrity of 3D printed polymer medical devices, such as custom implants [17].

Finally, HRI results indicate the utility of 3D printed phantoms for assessment of biophotonic device performance metrics such as penetration depth and minimum detectable concentration of an analyte or contrast agent. However, thorough characterization of phantoms from any new type of printer is likely needed before implementation. Future work will focus on developing 3D printed phantoms with more biologically relevant optical properties and image-derived morphology, as well as assessing long-term variations in polymer optical properties.

References

1. J. Pfefer and A. Agrawal, Proc. SPIE **8215**, 82150D (2012).
2. B. W. Pogue and M. S. Patterson, J. Biomed. Opt. **11**, 041102 (2006).
3. J. C. Ramella-Roman, S. A. Mathews, H. Kandimalla, A. Nabili, D. D. Duncan, S. A. D'Anna, S. M. Shah, and Q. D. Nguyen, Opt. Express **16**, 6170 (2008).
4. J. Baxi, W. Calhoun, Y. J. Sepah, D. X. Hammer, I. Ilev, T. J. Pfefer, Q. D. Nguyen, and A. Agrawal, J. Biomed. Opt. **19**, 021106 (2014).
5. R. Long, T. King, T. Akl, M. N. Ericson, M. Wilson, G. L. Cote, and M. J. McShane, Biomed. Opt. Express **2**, 1877 (2011).
6. F. Rengier, A. Mehndiratta, H. V. Tengg-Kobligk, C. M. Zechmann, R. Unterhinninghofen, H.-U. Kauczor, and F. L. Giesel, Int. J. CARS **5**, 335 (2010).
7. M. J. Burfeindt, T. J. Colgan, R. O. Mays, J. D. Shea, N. Behdad, B. D. Van Veen, and S. C. Hagness, IEEE Antennas Wireless Propagat. Lett. **11**, 1610 (2012).
8. S. M. Peltola, F. P. W. Melchels, D. W. Grijpma, and M. Kellomäki, Ann. Med. **40**, 268 (2008).
9. T. Nguyen, H. Le, M. Vo, Z. Wang, L. Luu, and J. Ramella-Roman, Biomed. Opt. Express **3**, 1200 (2012).
10. A.-K. Carton, P. Bakic, C. Ullberg, H. Derand, and A. D. A. Maidment, Med. Phys. **38**, 891 (2011).
11. S. A. Prahl, M. J. C. van Gemert, and A. J. Welch, Appl. Opt. **32**, 559 (1993).
12. E. K. Chan, B. Sorg, D. Protsenko, M. O'Neil, M. Motamedi, and A. J. Welch, IEEE J. Sel. Top. Quantum Electron. **2**, 943 (1996).
13. A. Yaroslavsky, P. Schulze, I. Yaroslavsky, R. Schober, F. Ulrich, and H. Schwarzmaier, Phys. Med. Biol. **47**, 2059 (2002).
14. M. Hammer, A. Roggan, D. Schweitzer, and G. Muller, Phys. Med. Biol. **40**, 963 (1995).
15. A. T. Luk, Y. Lin, B. Grimmond, A. Sood, E. E. Uzgiris, O. Nalcioglu, and G. Gulsen, Proc. SPIE **8574**, 85740K (2013).
16. N. Keshava, Lincoln Lab. J. **14**, 55 (2003).
17. D. A. Zopf, S. J. Hollister, M. E. Nelson, R. G. Ohye, and G. E. Green, N. Engl. J. Med. **368**, 2043 (2013).